The Laser calibration of the ATLAS Tile Calorimeter during the LHC run 1

You may also be interested in:

The ATLAS tile calorimeter: Commissioning and preparation for collisions
O Solovyanov and Atlas Tile Community

ATLAS Tile Calorimeter: simulation and validation of the response
Jana Faltova and the ATLAS Collaboration

Calorimeters: Key detectors for LHC physics
Egidio Longo

Event filter monitoring with the ATLAS tile calorimeter
L Fiorini and N Gollub

Time calibration of the ATLAS tile calorimeter using an integrated laser system
Björn Nordkvist and the Atlas Tile Calorimeter Collaboration

Towards Optimal Filtering on ARM for ATLAS Tile Calorimeter Front-End Processing
Mitchell A Cox

The response of the ATLAS Tile calorimeter to pions and protons in test beam and in GEANT4 Monte Carlo simulation
Margar Simonyan and the ATLAS Tile Calorimeter Group, ATLAS Collaboration

TECHNICAL REPORT

The Laser calibration of the ATLAS Tile Calorimeter during the LHC run 1

ATLAS Tile Calorimeter system

J. Abdallah,[20] C. Alexa,[29] Y. Amaral Coutinho,[37] S.P. Amor Dos Santos,[8,26] K.J. Anderson,[14]
G. Arabidze,[5] J.P. Araque,[26] A. Artamonov,[21] L. Asquith,[18] R. Astalos,[17] J. Backus Mayes,[32]
P. Bartos,[17] L. Batkova,[17] F. Bertolucci,[11] O. Bessidskaia Bylund,[36] A. Blanco Castro,[26]
T. Blazek,[17] C. Bohm,[36] D. Boumediene,[27] A. Boveia,[14] H. Brown,[7] E. Busato,[27] R. Calkins,[6]
D. Calvet,[27,*] S. Calvet,[27] R. Camacho Toro,[27] R. Caminal Armadans,[20] T. Carli,[2]
J. Carvalho,[8,26] M. Cascella,[11] N.F. Castro,[26,4,3] V. Cavasinni,[11] A.S. Cerqueira,[13]
R. Chadelas,[27] D. Chakraborty,[6] S. Chekanov,[18] X. Chen,[34] L. Chikovani,[12,†]
G. Choudalakis,[14] D. Cinca,[27] M. Ciubancan,[29] C. Clement,[36] S. Cole,[6] S. Constantinescu,[29]
T. Costin,[14] M. Crouau,[27] C. Crozatier,[27] C.-M. Cuciuc,[29]
M.J. Da Cunha Sargedas De Sousa,[15,26] S. Darmora,[7] T. Davidek,[16] T. Del Prete,[11] S. Dita,[29]
T. Djobava,[19] J. Dolejsi,[16] A. Dotti,[11] E. Dubreuil,[27] M. Dunford,[14] D. Eriksson,[36] S. Errede,[9]
D. Errede,[9] J. Faltova,[16] A. Farbin,[7] R. Febbraro,[27] P. Federic,[17] E.J. Feng,[18] A. Ferrer,[24]
M. Fiascaris,[14] M.C.N. Fiolhais,[8,26] L. Fiorini,[20] P. Francavilla,[20] E. Fullana Torregrosa,[2]
B. Galhardo,[8,26] K. Gellerstedt,[36] N. Ghodbane,[27] V. Giakoumopoulou,[31] V. Giangiobbe,[20]
N. Giokaris,[31] G.L. Glonti,[25] A. Gomes,[26,15] G. Gonzalez Parra,[20] P. Grenier,[32] S. Grinstein,[20]
Ph. Gris,[27] C. Guicheney,[27] H. Hakobyan,[38,†] A.S. Hard,[10] S. Harkusha,[1] L. Heelan,[7]
C. Helsens,[20] A.M. Henriques Correia,[2] Y. Hernández Jiménez,[24] C.M. Hernandez,[7]
E. Higón-Rodriguez,[24] M. Hurwitz,[14] N. Huseynov,[25] J. Huston,[5] I. Jen-La Plante,[14]
D. Jennens,[33] K.E. Johansson,[36] K. Jon-And,[36] P.M. Jorge,[15,26] A. Juste Rozas,[20] A. Kapliy,[14]
S.N. Karpov,[25] A.N. Karyukhin,[35] H. Khandanyan,[36] E. Khramov,[25] J. Khubua,[19] H. Kim,[36]
P. Klimek,[36] I. Korolkov,[20] A. Kruse,[10] Y. Kulchitsky,[1] Y.A. Kurochkin,[1] P. Lafarguette,[27]
D. Lambert,[27] T. LeCompte,[18] R. Leitner,[16] S. Leone,[11] H. Liao,[27] K. Lie,[9] M. Lokajicek,[23]
O. Lundberg,[36] P.J. Magalhaes Martins,[8,26] A. Maio,[26,15] M. Makouski,[35] J. Maneira,[15,26]
L. Manhaes de Andrade Filho,[37] A. Manousakis-Katsikakis,[31] B. Martin,[5] G. Mchedlidze,[19]
S. Meehan,[14] B.R. Mellado Garcia,[34] E. Meoni,[20] F.S. Merritt,[14] C. Meyer,[14] D.W. Miller,[14]
D.A. Milstead,[36] I.A. Minashvili,[25] L.M. Mir,[20] S. Molander,[36] J. Montejo Berlingen,[20]
M. Mosidze,[19] A.G. Myagkov,[35] S. Nemecek,[23] A.A. Nepomuceno,[37] D.H. Nguyen,[18]

---

*Corresponding author.

†Deceased.

V. Nikolaenko,[35] P. Nilsson,[7] L. Nodulman,[18] B. Nordkvist,[36] C.C. Ohm,[2] A. Olariu,[29]
L.F. Oleiro Seabra,[26] A. Onofre,[4,26] M.J. Oreglia,[14] D. Pallin,[27] D. Pantea,[29]
D. Paredes Hernandez,[27] M.I. Pedraza Morales,[10] R. Pedro,[15,26] F.M. Pedro Martins,[26]
H. Peng,[10] B. Penning,[14] J.E. Pilcher,[14] J. Pina,[26] V. Pleskot,[16] E. Plotnikova,[25] F. Podlyski,[27]
G.A. Popeneciu,[28] J. Poveda,[10] R. Pravahan,[7] L. Pribyl,[2] L.E. Price,[18] J. Proudfoot,[18]
J.G. Rocha de Lima,[6] C. Roda,[11] D. Roda Dos Santos,[23] S.M. Romano Saez,[27] V. Rossetti,[20]
A. Ruiz-Martinez,[24] N.A. Rusakovich,[25] B.M. Salvachua Ferrando,[18] C. Santoni,[27]
H. Santos,[26] J.G. Saraiva,[26] L.P. Says,[27] A. Schwartzman,[32] F. Scuri,[11] S. Shimizu,[2] J. Silva,[26]
S.B. Silverstein,[36] C.A. Solans,[24] A.A. Solodkov,[35] O.V. Solovyanov,[35] M. Spalla,[11]
R.W. Stanek,[18] E.A. Starchenko,[35] P. Starovoitov,[30] P. Stavina,[17] G. Stoicea,[29] A. Succurro,[20]
C. Suhr,[6] T. Sumida,[2] I. Sykora,[17] P. Tas,[16] A. Tavares Delgado,[15,26] S. Tokár,[17]
P.V. Tsiareshka,[1] V. Tsiskaridze,[19] V. Tudorache,[29] A. Tudorache,[29] J.M. Tuggle,[14]
M. Tylmad,[36] G. Usai,[7] A. Valero,[24] L. Valery,[27] E. Valladolid Gallego,[24] J.A. Valls Ferrer,[24]
F. Vazeille,[27] F. Veloso,[8,26] I. Vichou,[9,†] V.B. Vinogradov,[25] S. Viret,[27] M. Volpi,[20] C. Wang,[22]
Z. Weng,[22] A. White,[7] H.G. Wilkens,[2] S. Yanush,[30] R. Yoshida,[18] L. Zhang,[22] Y. Zhu,[10]
Z. Zinonos,[11] V. Zutshi,[6] T. Ženiš[17] and M.C. van Woerden[2]

[1]B.I. Stepanov Institute of Physics, National Academy of Sciences of Belarus,
  Minsk, Republic of Belarus

[2]CERN, Geneva, Switzerland

[3]Departamento de Física e Astronomia, Faculdade de Ciências, Universidade do Porto, Portugal

[4]Departamento de Fisica, Universidade do Minho, Braga, Portugal

[5]Department of Physics and Astronomy, Michigan State University,
  East Lansing MI, United States of America

[6]Department of Physics, Northern Illinois University, DeKalb IL, United States of America

[7]Department of Physics, The University of Texas at Arlington, Arlington TX, United States of America

[8]Department of Physics, University of Coimbra, Coimbra, Portugal

[9]Department of Physics, University of Illinois, Urbana IL, United States of America

[10]Department of Physics, University of Wisconsin, Madison WI, United States of America

[11]Dipartimento di Fisica E. Fermi, Università di Pisa, Pisa, Italy

[12]E. Andronikashvili Institute of Physics, Iv. Javakhishvili Tbilisi State University, Tbilisi, Georgia

[13]Electrical Circuits Department, Federal University of Juiz de Fora (UFJF), Juiz de Fora, Brazil

[14]Enrico Fermi Institute, University of Chicago, Chicago IL, United States of America

[15]Faculdade de Ciências, Universidade de Lisboa, Lisboa, Portugal

[16]Faculty of Mathematics and Physics, Charles University in Prague, Praha, Czech Republic

[17]Faculty of Mathematics, Physics & Informatics, Comenius University, Bratislava, Slovak Republic

[18]High Energy Physics Division, Argonne National Laboratory, Argonne IL, United States of America

[19]High Energy Physics Institute, Tbilisi State University, Tbilisi, Georgia

[20]Institut de Física d'Altes Energies (IFAE), The Barcelona Institute of Science and Technology,
  Barcelona, Spain

[21]Institute for Theoretical and Experimental Physics (ITEP), Moscow, Russia

[22]Institute of Physics, Academia Sinica, Taipei, Taiwan

[23]Institute of Physics, Academy of Sciences of the Czech Republic, Praha, Czech Republic

[24]*Instituto de Física Corpuscular (IFIC) and Departamento de Física Atómica,
Molecular y Nuclear and Departamento de Ingeniería Electrónica and Instituto de Microelectrónica de
Barcelona (IMB-CNM), University of Valencia and CSIC, Valencia, Spain*

[25]*Joint Institute for Nuclear Research, JINR Dubna, Dubna, Russia*

[26]*Laboratório de Instrumentação e Física Experimental de Partículas - LIP, Lisboa, Portugal*

[27]*Laboratoire de Physique Corpusculaire,
Clermont Université and Université Blaise Pascal and CNRS/IN2P3,
Clermont-Ferrand, France*

[28]*National Institute for Research and Development of Isotopic and Molecular Technologies,
Physics Department, Cluj Napoca, Romania*

[29]*National Institute of Physics and Nuclear Engineering, Bucharest, Romania*

[30]*National Scientific and Educational Centre for Particle and High Energy Physics,
Minsk, Republic of Belarus*

[31]*Physics Department, University of Athens, Athens, Greece*

[32]*SLAC National Accelerator Laboratory, Stanford CA, United States of America*

[33]*School of Physics, University of Melbourne, Victoria, Australia*

[34]*School of Physics, University of the Witwatersrand, Johannesburg, South Africa*

[35]*State Research Center Institute for High Energy Physics (Protvino), NRC KI, Russia*

[36]*The Oskar Klein Centre, Stockholm, Sweden*

[37]*Universidade Federal do Rio De Janeiro COPPE/EE/IF, Rio de Janeiro, Brazil*

[38]*Yerevan Physics Institute, Yerevan, Armenia*

E-mail: calvet@in2p3.fr

ABSTRACT: This article describes the Laser calibration system of the ATLAS hadronic Tile Calorimeter that has been used during the run 1 of the LHC. First, the stability of the system associated readout electronics is studied. It is found to be stable with variations smaller than 0.6 %. Then, the method developed to compute the calibration constants, to correct for the variations of the gain of the calorimeter photomultipliers, is described. These constants were determined with a statistical uncertainty of 0.3 % and a systematic uncertainty of 0.2 % for the central part of the calorimeter and 0.5 % for the end-caps. Finally, the detection and correction of timing mis-configuration of the Tile Calorimeter using the Laser system are also presented.

Contents

The ATLAS Tile Calorimeter [1, 2] (TileCal) is the central hadronic calorimeter of the ATLAS experiment at the Large Hadron Collider (LHC) at CERN. The TileCal is a sampling calorimeter whose operation is based on the detection of scintillation light using photomultiplier tubes (PMTs). On average, around 30 % of the total energy of jets from quark and gluon fragmentation is deposited in the TileCal. It therefore plays an important role for the precise reconstruction of the kinematics of the physics event. The control of its stability, within 1 %, and resolution is important for a
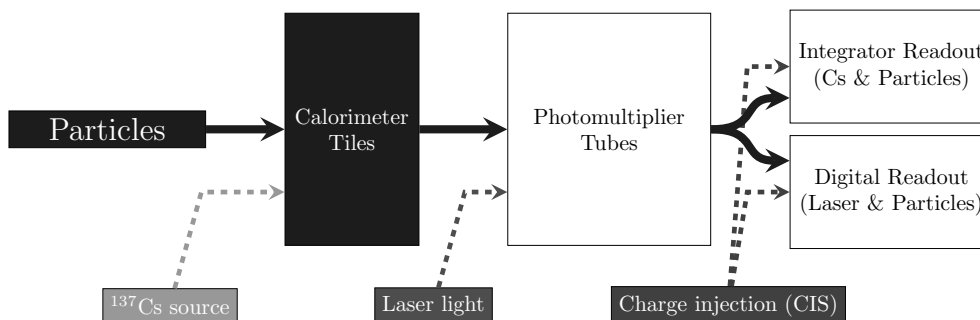
Figure 1. Flow diagram of the readout signal paths of the different TileCal calibration systems.

correct jet and missing transverse energy reconstruction in ATLAS.[1] In order to obtain a precise and stable measurement of the energy deposited in the calorimeter, it is mandatory to precisely monitor any variation of the gain[2] of the PMTs and, if needed, correct for these variations. Several complementary hardware calibration systems have therefore been included in the TileCal design (see figure 1), one of them being the Laser system described in this article.

The calorimeter is briefly described in section 1, and the Laser system as it was operational during run 1 of the LHC is detailed in section 2. A major upgrade of this system was performed in 2014, but falls outside the scope of this article. The study of the stability of the Laser electronics is discussed in section 3 before the description of the calibration procedure in section 4. Timing mis-configuration detection and correction are detailed in section 5 while monitoring of pathological calorimeter channels is briefly described in section 6. Finally, conclusions are drawn in section 7.

1 The ATLAS Tile Calorimeter

The ATLAS detector is made of a central part, called the barrel, and two endcaps. In the barrel, the TileCal is the only hadronic calorimeter of ATLAS. In the endcaps, TileCal constitutes the external part of the hadronic calorimeter, the internal part using the liquid argon technology. The part of TileCal that is in the ATLAS barrel is called the *long barrel* (LB), while the parts that are in the endcaps are called the *extended barrels* (EB).

The Tile Calorimeter is the result of a long process of R&D and construction. The Technical Design Report [3] has been completed in 1995 and the construction of the mechanical part ended in 2006. After a period of operation using cosmic muons, the TileCal was ready in 2009 to record the first LHC proton-proton collisions.

1.1 Mechanical aspects

TileCal is a non-compensating sampling calorimeter made of steel plates that act as absorber and provide mechanical structure into which the active scintillating tiles are inserted. Charged particles

---

[1]The designed energy resolution of jets is $\sigma/E = 50\%/\sqrt{E(\text{GeV})} \oplus 3\%$ and the systematic uncertainty on the jet energy scale in ATLAS must be at most 1 %. See details in [2].

[2]What is really monitored is the product of the PMT photocathode quantum efficiency by the PMT gain. In this article, it is assumed that any quantum efficiency variation is negligible over the typical time scale of a few months and therefore the term *PMT gain* is used instead of the product.

going through the tiles produce scintillation light that is collected by two wavelength-shifting (WLS) fibres, on each side of a tile. These fibres are then grouped in bundles to form cells, organised in three radial layers, as depicted in figure 2, thus achieving a granularity of about 0.1 in η[3] for the layers A and BC (the closest to the collision point) and around 0.2 in the outermost layer. Azimuthally, the detector is segmented in 64 wedge-shaped modules (see figure 3), thus achieving a granularity of $\Delta\phi = 0.1$. The E cells are non-standard calorimeter cells made of single large scintillators. Their aim is to measure the energy of particles lost in the inactive material located in front of the TileCal. In total, there are 5182 cells.

In addition, 16 large scintillator plates are located between the barrel and the endcaps, the Minimum Bias Trigger Scintillators (MBTS). They are mainly used in the ATLAS low luminosity trigger. Although they are not TileCal cells, their readout is performed by dedicated PMTs of the TileCal system, that were originally planned to be connected to 8 pairs of E3 and E4 cells.

1.2 Detector readout

Each fibre bundle, usually corresponding to one side of a cell, is read out by a photomultiplier tube: each standard cell is thus read out by two PMTs, the E cells being read out by a single PMT. Therefore, there are 9852 PMTs in total. The electric pulses generated by the PMTs are shaped [4] and digitised [5] at 40 MHz with two different gains, with a ratio of 64, in order to achieve a good precision in a wide energy range. These samples are then stored in a pipeline memory until the level-1 trigger decision is taken (ATLAS has a three-level trigger system, the first level giving a decision in 2.5 μs during which the data are kept in the front-end electronics). If the decision is positive, seven samples, in time with the signal and with appropriate gain giving the best precision on the pulse amplitude, are sent to the off-detector electronics (Read Out Drivers or RODs [6]). The amplitude of the signal is reconstructed as the weighted linear combination of the digitised signal samples, using an optimal filtering method [7, 8].

In parallel, the output of each PMT is also integrated over approximately 14 ms using an analog integration system, during Cesium calibrations (see below and figure 1) and also to measure the PMT current induced by minimum bias proton-proton collisions.

1.3 Hardware calibration systems

Three different and complementary hardware calibration systems have been integrated in the TileCal design: the Cesium system [9], the Laser system and the Charge Injection System (CIS) [4] (see figure 1).

About once or twice a month, a radioactive ^{137}Cs source scans most[4] TileCal cells, measuring the response of the tiles, including the WLS fibres and the PMTs, to a known amount of deposited energy. For this Cesium calibration, the analog integrator is used instead of the digital readout: it is therefore not sensitive to potential variations of the gain of the readout electronics used for physics.

---

[3]ATLAS uses a right-handed coordinate system with its origin at the nominal interaction point (IP) in the centre of the detector and the z-axis coinciding with the axis of the beam pipe. The x-axis points from the IP to the centre of the LHC ring, and the y-axis points upward. Cylindrical coordinates (r,ϕ) are used in the transverse plane, ϕ being the azimuthal angle around the beam pipe. The pseudorapidity is defined in terms of the polar angle θ as $\eta = -\ln\tan(\theta/2)$.

[4]For mechanical reasons, the special cells E3 and E4 cannot be calibrated by the Cesium source, see figure 2 and section 4.4 for more details.
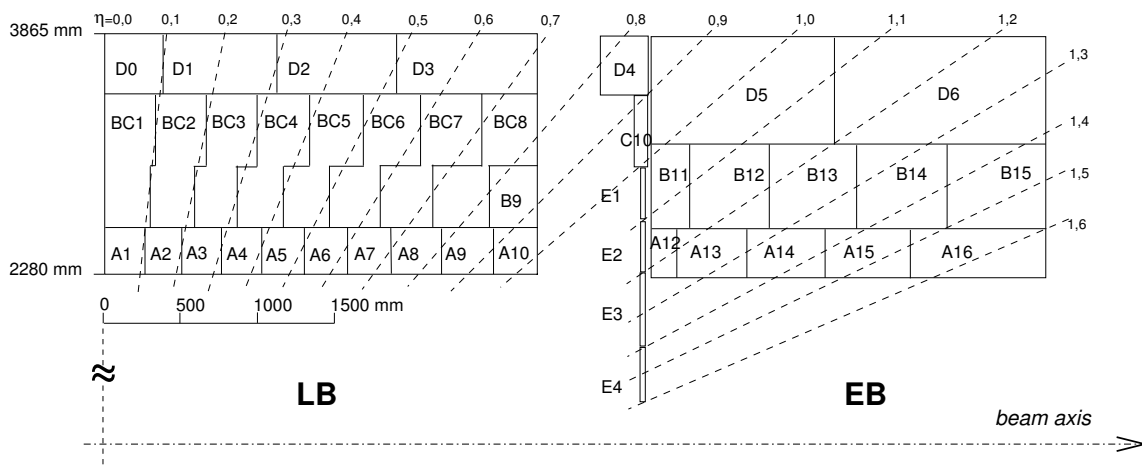
Figure 2. Schematic of the cell layout in a plane parallel to the beam axis, showing only positive η side (the detector being symmetric with respect to $\eta = 0$). The three radial layers (A, BC and D) are also visible. Special scintillators, called gap (E1 and E2) and crack (E3 and E4) cells, are located between the barrel and the endcap.
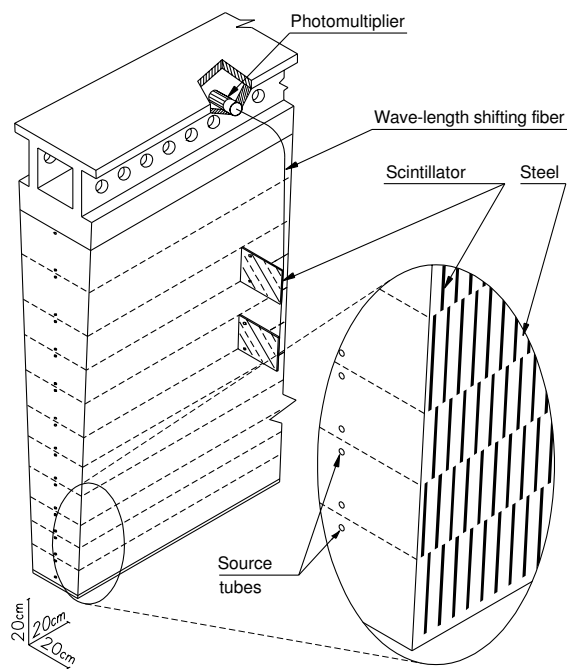
Figure 3. Sketch of a TileCal module, showing the light readout path between the scintillating tiles and the photomultiplier tubes (PMTs).

– 4 –
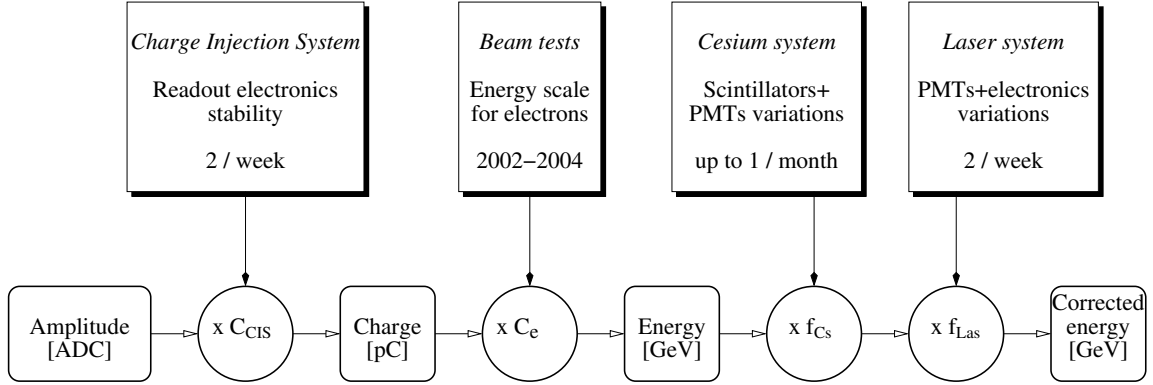
Figure 4. Diagram of the contributions of the hardware calibration systems to the energy reconstruction.

The Laser calibration is performed about twice a week and allows monitoring the stability of the PMT gain between two Cesium calibrations by illuminating all PMTs with a Laser pulse of a known intensity. For this calibration, the same readout electronics as for physics is used and is therefore also monitored. This calibration is described in detail in the next sections.

During the CIS calibrations, performed about twice a week, a known electric charge is injected into the readout electronics chain, simulating a PMT output pulse. It is used to measure the conversion factor from ADC-counts to pico-Coulomb (pC) and also to monitor the linearity of the ADCs.

1.4 Energy reconstruction

In order to measure correctly the energy, several effects must be taken into account, using the calibration systems described previously as well as results from tests using special beams of particles (see figure 4). Hence, for each PMT, the energy is reconstructed as

$$E = A_{\text{opt}} \times C_{\text{CIS}} \times C_e \times f_{\text{Cs}} \times f_{\text{Las}} \tag{1.1}$$

where A_{opt} is the amplitude in ADC counts computed by the optimal filtering method, C_{CIS} is the ADC→pC conversion factor measured by the CIS, C_e is the pC→GeV conversion factor defining the energy scale as measured with electron beams in past beam tests [10] and f_{Cs} and f_{Las} are correction factors extracted from the Cesium and Laser calibrations. The Cesium calibration is able to correct the residual non-uniformities after the gain equalisation of all channels and thus to preserve the energy scale of the calorimeter that was determined during the beam tests. The Laser calibration allows keeping stable this energy scale between two Cesium scans and is therefore relative to the Laser calibration immediately consecutive to the last Cesium calibration. The cell energy is the sum of the energies from the two PMTs connected to this cell.

The computation of the Laser calibration constants f_{Las} will be described in the next sections.

2 The Laser calibration system

The first prototype of the Laser system has been built in 1993 and the first tests with a prototype module of the calorimeter were performed in October 1994 [11]. A second prototype was then built and tested in 1997 [12]. After several improvements, a first version of the system has been
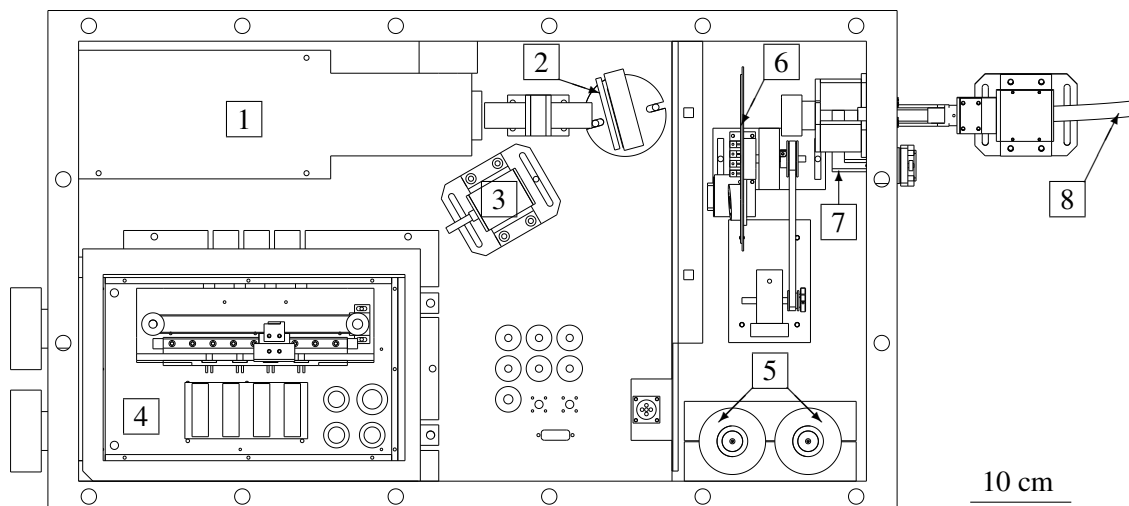
Figure 5. Sketch of the Laser box, showing the Laser head (1), the semi-reflecting mirror (2), the light mixer (3) that distributes the light to the photodiodes box (4) and the two PMTs (5), the filter wheel (6), the shutter (7) and the output liquid light guide (8).

used during the qualification of the TileCal modules using particle beams [10]. Finally, the system described in the following paragraphs was installed in its definitive location in 2008, in time for the calibration of TileCal before the first LHC collisions. After several years of running, the current Laser system has been upgraded in October 2014 for the LHC run 2, starting in 2015. This new system includes a new Laser source, new optical components and new electronic boards, and is not described in this article.

The Laser system contains of course a Laser source but also other components. Because the actual intensity of the pulses has variations of approximately 5 %, the system includes dedicated photodiodes to precisely measure the intensity of each pulse. It also includes a tunable attenuation system to cover the whole TileCal PMTs dynamic range (100 MeV to 1.5 TeV per PMT).

The Laser system consists of a Laser pump, the so-called Laser box, a light distribution system and several electronic components in a VME crate to control and monitor the system. The Laser box (see figure 5) contains the Laser head, two photomultipliers, the so-called photodiodes box, a semi-reflecting mirror, a filter wheel and a shutter. The photodiodes box contains four PIN photodiodes from Hamamatsu [13] with their amplifiers and shapers. These components are located in the USA15 cavern that hosts the back-end electronics, and that is close to the main ATLAS cavern.

The Laser system can be operated in four different modes, divided in two categories: three internal calibration modes and one Laser mode.

Internal calibration modes: the aim of these modes is to calibrate and monitor the Laser system electronics, without any Laser light emission. There are three different calibration modes:

- two to measure the characteristics of the electronics: linearity (Linearity mode), noise and pedestal level (Pedestals mode);

- one to calibrate the photodiodes, with an embedded radioactive source (Alpha mode).

– 6 –

Laser mode: this mode represents the main operation mode, in order to calibrate the TileCal PMTs using Laser light.

2.1 Choice of the light source

In order to synchronise all the TileCal channels, it is mandatory to be able to send simultaneously a single light pulse to the 9852 PMTs, which requires a powerful light source such as a Laser. Pulse shape requirements (~10 ns pulse width) has driven our choice toward a commercial Q-switched DPSS (Diode-Pumped Solid State) Laser manufactured by SPECTRA-PHYSICS. This is a frequency-doubled infrared Laser emitting a 532 nm green light beam, this wavelength being close to the one of the light coming out of the WLS fibres (480 nm). It delivers 10 to 15 ns pulses of a few μJ maximum energy, which is sufficient to saturate all TileCal channels, and thus to test their full dynamic range. Moreover, the pulse shape is sufficiently similar to the shape of physics signals, so that the optimal filtering method does not have to be adapted. The delay between triggering and actual light emission is of the order of 1.2 μs, which depends on the pulse energy in a window of about 60 ns; and a jitter of 25 ns due to the internal 40 MHz clock of the Laser source electronics.

2.2 Laser light path

The light emitted by the Laser head passes first through a semi-reflecting mirror (commercial metallic neutral density filter). About 10 % of the light is redirected towards a specific calibration system in order to measure precisely the amount of light that has been emitted, with a photodiode, and also to precisely measure the time when the pulse was emitted with two PMTs.

The light that passes through the semi-reflecting mirror then goes through a rotating filter wheel, which is used to attenuate the outgoing light. This wheel contains seven metallic neutral density filters, each one applying a specific attenuation factor (from 3 to 1000). The filter wheel contains also an empty slot in order to reach the maximum intensity.

Downstream of the filter wheel, a shutter allows controlling whether the light is sent to TileCal or not. When this shutter is open, the light enters a 1 m long light guide with a 5 mm diameter liquid core that acts as a first beam expander (see figure 6). The liquid light guide has been chosen for its large acceptance cone, high transmittance and very good resistance to powerfull light pulses. At the output of the liquid light guide, the light enters in the beam expander and light splitter [14] (see figure 7), where the Laser beam is first enlarged by means of a divergent lens followed by a convergent one in order to obtain a parallel light beam. In order to avoid any speckle effects, the beam then goes into a coherence-killing light-mixer, made of a parallelepipedic PMMA block. At the output of this block, the light is transmitted to a bundle of 400 clear optical fibres (Mitsubishi ESKA GH4001).

In order to further improve the splitting uniformity, the amount of light transmitted to the 400 secondary fibres can be varied with adjustable distance optical connectors [15]. From these 400 outputs, 384 of them are connected to 80 m long clear fibres of similar model, that bring the light from the USA15 cavern to the TileCal modules. Inside a module, each clear fibre is connected to 17 (EB) or 48 (LB) fibres of the same type but with lengths varying between 0.5 and 6 m; each of these fibres reaching one PMT. The light splitting is performed by the mean of an empty anodized aluminium tube: the incoming beam expands and reflects on the inner wall of the tube before
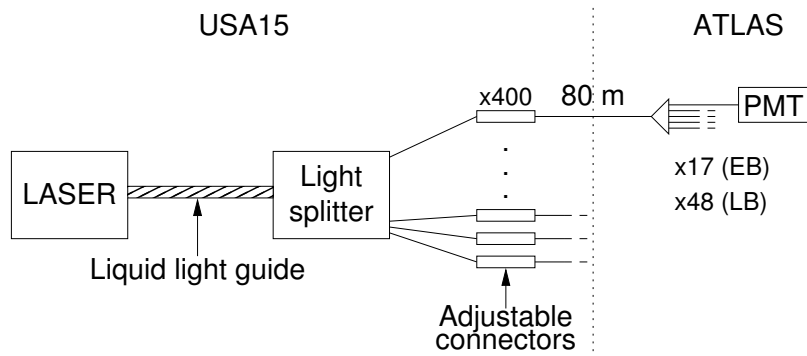
Figure 6. Sketch of the light splitting scheme. The main light splitter distributes the light to 400 optical fibres, 256 for the two extended barrels, 128 for the long barrel and 16 spares. In each module, the secondary light splitter distributes the light to 17 (EB) or 48 (LB) fibres, connected to 16 (EB) or 45 (LB) photomultipliers.
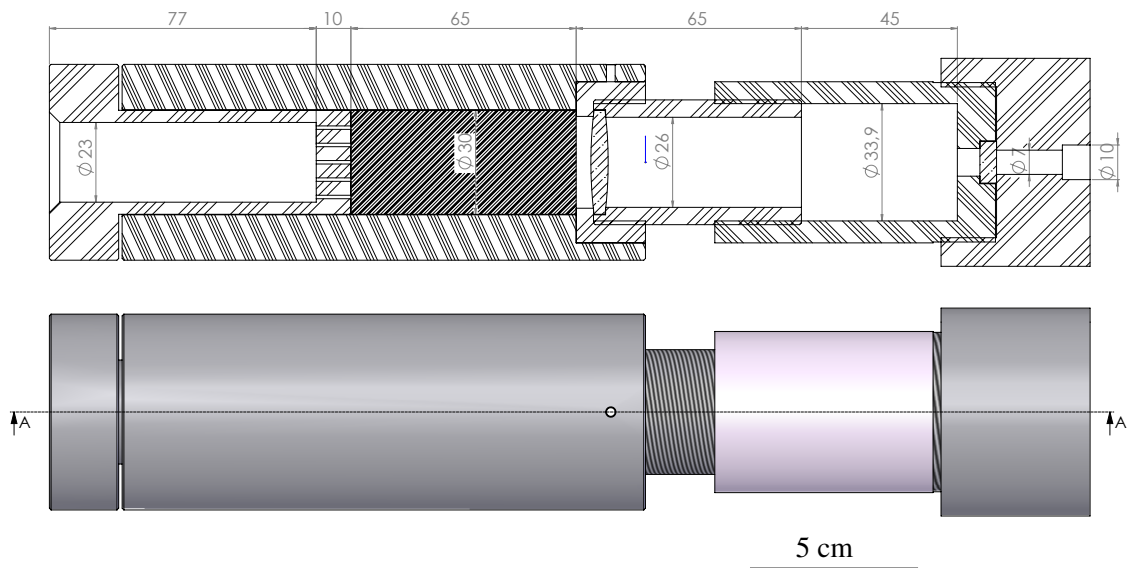
Figure 7. Sketch of the beam expander and light splitter. The light enters from the right hand-side of the figure.

reaching the bundle of output fibres. These tubes are 26 mm (respectively 40 mm) long with an internal diameter of 6 mm (10 mm) in the EB (LB). In total, each endcap module is fed by two 80 m fibres (16 PMTs per fibre) and each barrel module is fed by two fibres (45 PMTs per fibre). It should be noted that the light splitters located in the modules can not be tuned.

Connected to the adjustable connectors, three additional fibres go back inside the Laser box in order to measure the intensity of the light pulses downstream of the filter wheel. Due to the large range of available attenuations (from 1 to 1000), the light sent to these three photodiodes has been tuned in order to always have a measurable signal in at least one of them.

2.3   Radioactive source

The four photodiodes are located in a special box in which temperature and humidity levels are monitored and controlled by Peltier elements and a dry air flow. This box also contains a 16 mm

diameter radioactive source of ^{241}Am, releasing mostly α particles of 5.6 MeV with an activity of 3.7 kBq. This source provides an absolute calibration (independent from the Laser source) of each photodiode. In order to calibrate all the diodes, the source can be moved along them into the box.

2.4 Electronics

The VME 6U crate contains a VME processor, on which the software interface between the system and the ATLAS data acquisition system (DAQ) is running, and several custom-made electronic boards. The main boards that are needed for the data acquisition are described in the following paragraphs and can be seen on figure 8.

The LastQDC board is an eight channels charge Analog to Digital Converter, for the digitisation of the signal coming from the four photodiodes and the two photomultipliers. It has a resolution of 11 bits with a maximum range of 200 pC.

The LilasII board provides two distinct functions. The first function is a charge injection system used in the Linearity mode, with a 16-bit Digital to Analog Converter (DAC) producing a maximum output of 10 V that is injected in a 1 pF capacitor. The second function is an interface between the TileCal calibration requests system (Shaft[5]) and Slama, containing mostly counters to know precisely how many requests were sent by Shaft and by Slama.

The Slama board is the main component of the system, producing signals to control other components like the LastQDC, LilasII or the Laser pump. It contains three FPGAs (Altera ACEX EP1K300QC208): one is devoted to the VME communication, the second one to the communication with LastROD via a dedicated bus, and the last one to the management of the Laser pump and the production of the various electronic signals that are described in the next sections. This board contains also two 15-bit Time to Digital Converters (TDC) with a resolution of 250 ps. The internal clock of Slama has a frequency of 80 MHz, either from an internal oscillator or provided by LastROD (see hereafter).

The LastROD board is the dedicated Read Out Driver (ROD) of the Laser system, included in the ATLAS trigger and data acquisition system. It receives timing and trigger information from the standard ATLAS TTC systems, via an optical fibre connected to a TTCrq mezzanine board [16]. This mezzanine includes a QPLL that provides 40 MHz and 80 MHz clocks synchronised to the LHC clock. LastROD also sends the data to the ATLAS data acquisition computers (ROS), using another mezzanine board named HOLA [17], that contains a 2.5 Gbps optical link. The various functions of LastROD are implemented in four FPGAs (Altera Cyclone I EP1C12Q240C6N): the first one manages the communication with the TTCrq mezzanine, the second one the communication with the HOLA board, the third one is the VME decoder and the last one is devoted to the communication with the Slama and LastQDC boards via the dedicated bus.

Two other custom VME boards are needed to control the movements of the filter wheel and the radioactive source, and to monitor the low and high voltages, temperatures and humidity levels.

2.5 Operating in internal calibration modes

Operating the Laser system in one of the three internal calibration modes requires only a sub-set of the Laser system hardware.

---

[5]The Shaft board is also a VME board but it is not located in the Laser VME crate, as it is not only used by the Laser system but also by the CIS and the minimum bias current measurement system. This is the board that defines when the various systems must be triggered.
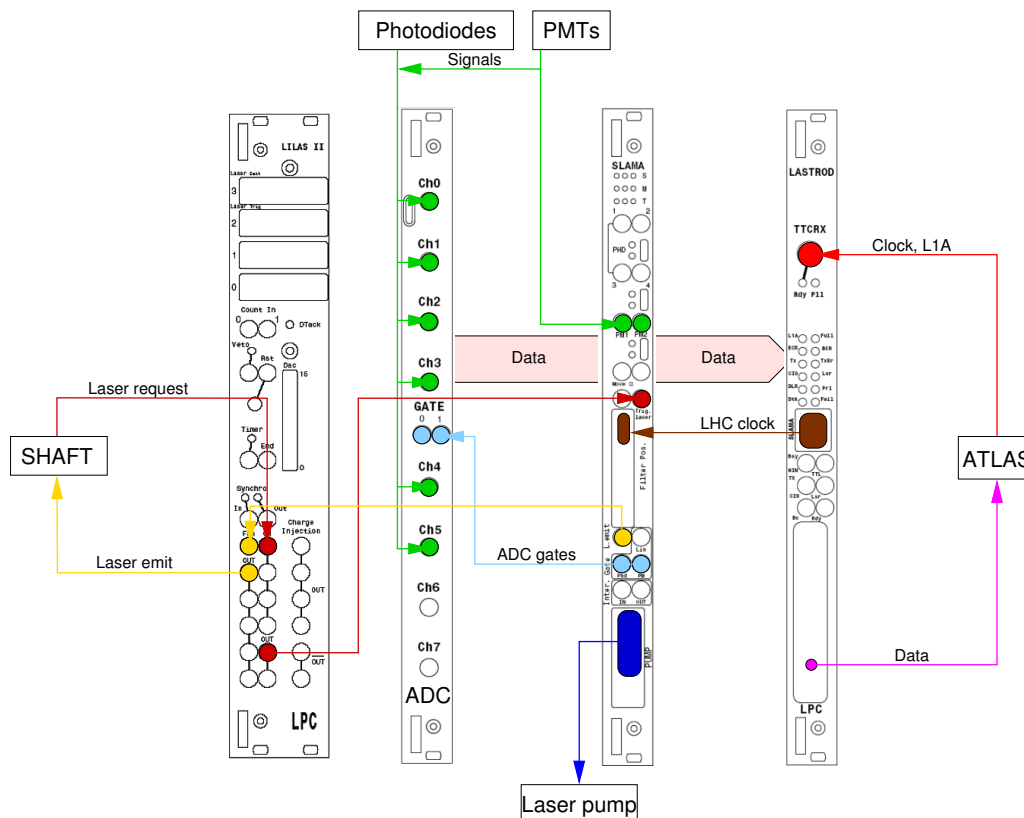
Figure 8. Laser system electronic boards involved in the Laser mode. The interactions between the various components are also shown. The board labelled ADC is the LastQDC board.

Pedestals mode. The aim of this mode is to record a high number of events without any energy in the photodiodes and the photomultipliers (neither from the Laser nor from the radioactive source). Slama generates a random gate for the LastQDC.

Alpha mode. In this mode, the α radioactive source is moved in the photodiodes box, in front of each photodiode. The signals coming out of the four photodiodes are fed into Slama, where they generate an internal trigger if at least one of them is above a given threshold. This internal trigger generates the gate needed by the LastQDC to digitise the delayed photodiodes signals: for each event, only one photodiode contains energy from the α radiation (see figure 9). In very rare cases, two α particles hit the photodiode within the same digitisation gate (as can be seen above ADC≃1000 in figure 9) but the effect is negligible. The large dispersion of the α spectrum is due to the absence of collimation of the α particles, resulting in a wide range of incidence angles[6] for the particles hitting the photodiode.

---

[6]The source and the photodiode have surfaces of approximately 200 mm^2 and they are separated by about 1 mm. Particles emitted perpendicular to the source travel a very short distance in the air gap and loose a very small amount of energy, while particles emitted almost parallel to the source travel much longer distances and therefore loose much more energy.
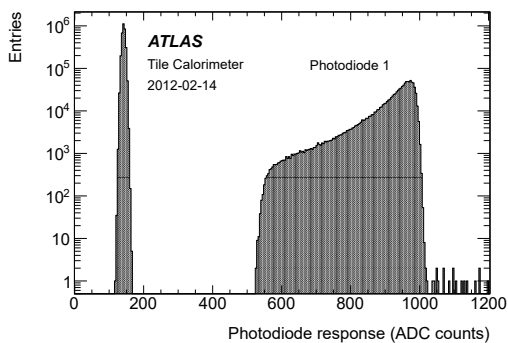
Figure 9. Example of distribution of the photo-diode response in the Alpha mode. Data around ADC=170 were taken while the radioactive source was in front of the other photodiodes, data between 500 and 1000 correspond to the α spectrum.
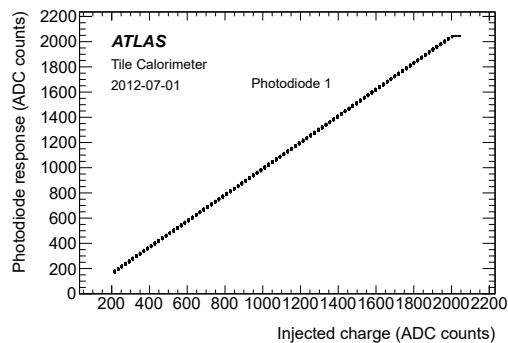
Figure 10. Example of photodiode response as a function of the measured injected charge in the Linearity mode. The saturation at high value of the photodiode response is an effect due to the ADC, not to the photodiode itself.

Linearity mode. This mode allows measuring the linearity of the photodiodes electronics (amplifier, shaper and ADC): a tunable electric charge is injected in this electronics (downstream of the photodiodes), the response of the photodiodes electronics and the injected charge are recorded (see figure 10).

2.6 Operating in Laser mode

The Laser system is operated in the Laser mode for two data-taking situations:

- dedicated calibration runs, when TileCal is operated independently of the rest of ATLAS and all events are Laser calibration events;

- standard physics runs, when TileCal is synchronised with the other ATLAS sub-detectors. In this configuration, the Laser pulses are emitted only during a dedicated period of the LHC orbit, in which it is ensured there are no collisions (see figure 12.2 of reference [18]), in order to separate physics events from calibration events.

The main difficulty in this mode is the timing. First, the Laser system must be synchronised with the other TileCal components, so that the events recorded in TileCal correspond to the events when the Laser pulse is emitted. Second, during standard physics runs, the Laser pulses must not be emitted during proton-proton collisions. In order to achieve these two goals, the Laser system is operated as a slave of the SHAFT board. The frequency at which the Laser pulses are emitted is about 1 kHz in the calibration runs and 1 Hz in the physics runs.

Operating in Laser mode requires most of the components, in particular the interfaces with ATLAS. The various boards located in the Laser VME crate that are needed in this mode can be seen in figure 8, together with their interactions.

The SHAFT board is programmed to send a request to the Laser system at a fixed time with respect to the beginning of the LHC orbit. Depending on the required frequency, this signal is only sent during selected orbits. When SLAMA receives this signal, it triggers a Laser pulse by the mean
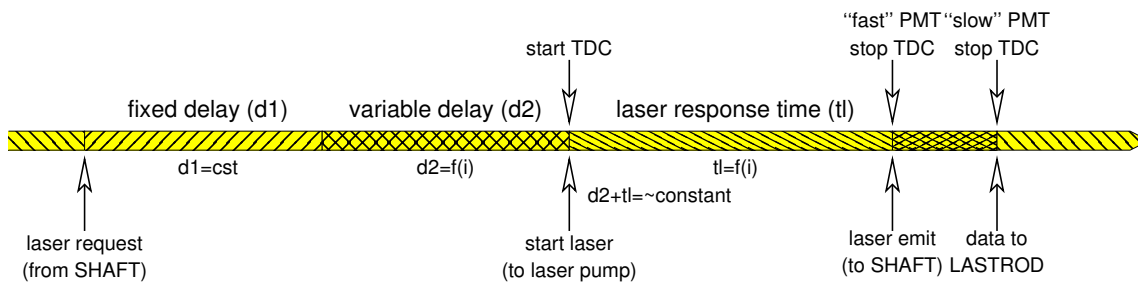
Figure 11. Sequence of signals to trigger a Laser pulse. The time (tl) between the reception of the trigger signal by the Laser pump and the pulse emission depends on the pulse intensity. The programmable delay (d2) is chosen as a function of the intensity in order to keep d2+tl constant.

of a signal sent to the Laser pump together with a DAC level to set the required Laser intensity. However, a small delay occurs between the pump triggering and the emission of the Laser pulse, and this delay is dependent on the pulse intensity. In order to compensate for this variable delay, SLAMA sends the trigger signal to the Laser pump only after a programmable time, by steps of 12.5 ns, as explained in figure 11.

The gates needed by the LASTQDC to digitise the photodiodes response are then produced by SLAMA from the response of one of the Laser box photomultipliers. Using its TDC and the signal from these photomultipliers, SLAMA also measures the time needed by the Laser pulse to be emitted. In order to get relevant time values, the internal 80 MHz SLAMA clock is the one that is produced by LASTROD, which is synchronised with the LHC clock.

Once SLAMA has detected that the pulse is correctly emitted, it generates a signal back to SHAFT that then sends a Laser calibration request to the ATLAS central trigger processor. This request is sent to SHAFT when the pulse is emitted in order to synchronise the pulse emission and the readout of TileCal. Then, a level-1 trigger (L1A) signal associated to this Laser event is distributed to the whole ATLAS detector, together with the TileCal Laser calibration trigger type (TT).

Finally, when a L1A is received by LASTROD, associated with the Laser TT, it sends to the ATLAS DAQ the amplitude of the Laser light, measured by the photodiodes, the time measured by the TDC, the average and RMS of the reponses measured during the last Pedestals and Alpha runs, as well as the state of the system (filter wheel position, shutter state, temperature and humidity in the Laser box, status of the power supplies). All this information is then available for offline analysis.

3 Stability of the electronics

Before any use of the Laser system to calibrate the TileCal, it is necessary to monitor the behaviour of its readout electronics and in particular the photodiodes. This is done in two steps: the first step is a measurement of the electronics characteristics when no energy is deposited in the photodiodes (no Laser light pulse nor α particle), the second step is a calibration of the photodiodes response using the radioactive source. These two steps are performed using the Pedestals and Alpha internal calibration modes, that are taken regularly.

3.1 Characteristics of the electronics

Each readout channel can be characterised by two numbers: its noise and its pedestal. The noise can be measured as the RMS of the distribution of the responses when no energy is recorded in the channel. The pedestal is the average response in the absence of deposited energy: its value is very important because it must be subtracted from the response of each channel, in order to obtain a response that is directly proportional to the intensity of the Laser pulses.

Both the pedestal and noise can be measured in the Pedestals runs and in the Alpha runs. Indeed, in the Alpha runs, for each event, only one photodiode is hit by an α particle, thus the three other photodiodes contain no energy; in this case, the pedestal and noise levels can be measured. It is also very important for the photodiodes calibration to make sure that the pedestal and noise are the same in the Pedestals and Alpha runs, in particular that there is no cross-talk between the channels when some energy is deposited in a photodiode.

The stability of the electronics has been studied during the LHC data taking periods of 2011, 2012 and 2013, from February 2011 to February 2013. Figure 12 shows the evolution of the pedestal measured in the Pedestals runs (P_{Ped}) and in the Alpha runs (P_α), together with the ratio $R^{Ped}_{\alpha/Ped} = P_\alpha/P_{Ped}$, for photodiode 1 (similar results are obtained for the three other photodiodes). The vertical dashed lines separate the two years in four periods, named A to D, that correspond to stable conditions separated by hardware interventions on the system. In particular, in March 31st 2011 (between periods A and B), a new version of the photodiodes amplifiers was installed, allowing to switch off photodiodes collecting an amount of light sufficient to saturate the electronics and thus generating cross-talk with the other channels. The second important intervention, in July 6th 2011 (between periods B and C), was a change in the photodiodes amplifiers grounding scheme in order to further reduce the cross-talk between channels. As can be seen in figure 12, the pedestals measured in Pedestals runs and in Alpha runs are similar (the ratio $R^{Ped}_{\alpha/Ped}$ is very close to 1 and is stable) during periods C and D, thus showing that the cross-talk has been reduced to a negligible value. This means that the pedestal measured in Pedestals runs can be safely subtracted from the measured response of the photodiodes in Alpha runs.

Figure 13 shows the evolution of the noise measured in the Pedestals runs (RMS_{Ped}) and in the Alpha runs (RMS_α), together with the ratio $R^{RMS}_{\alpha/Ped} = RMS_\alpha/RMS_{Ped}$. The change of grounding scheme in July 2011 significantly improved the electronic noise. Moreover, the noise is similar in the Pedestals and in the Alpha runs: $R^{RMS}_{\alpha/Ped} \sim 1$ with variations well within ± 5 %.

The linearity of the readout electronics can be measured by injecting a known charge in the photodiodes amplifiers and varying this charge over the full dynamic range (see figure 10). Using dedicated Linearity runs, the difference between the electronics response and a straight line varies within ± 1 %, with an RMS of 0.2 %.

Finally, using standalone Laser runs during which the shutter was closed, it was also possible to measure the pedestal and noise of the channels connected to the three photodiodes that see the light after the light splitter, but in a condition similar to a standard Laser run (Laser pump on and light pulses seen by the photodiode 1). The pedestal variation with respect to standard Pedestals runs is less than 1.5 % and the noise differs[7] by less than 5 %. This ensures that no significant cross-talk between photodiodes is observed during Laser runs.

---

[7]It must be noted that the noise is not systematically higher during Laser runs, but sometimes higher sometimes lower, as in Alpha runs.
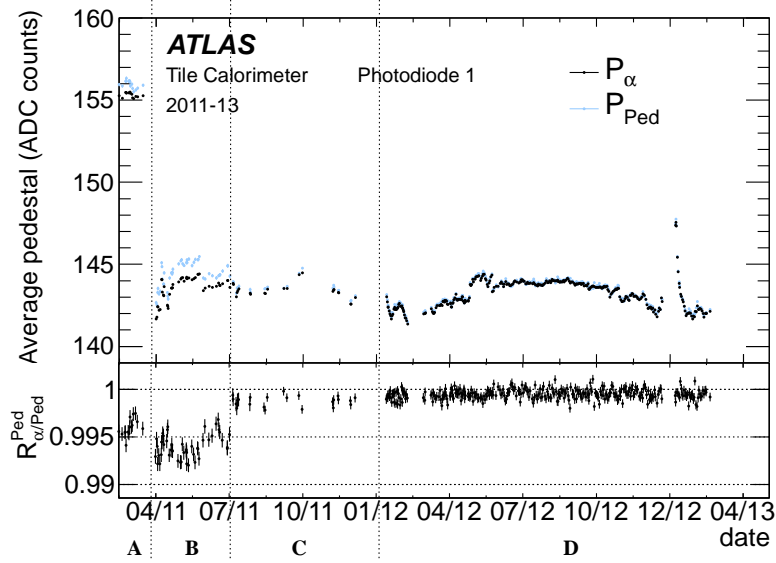
Figure 12. Evolution of the pedestal value measured in the Pedestals runs and in the Alpha runs, and their ratio for the first photodiode from February 2011 to February 2013. The error bars represent the statistical uncertainties on the averages and the ratios. The large variation early 2013 is due to the stabilisation of the readout electronics after the end-of-year shutdown, during which all systems were off.
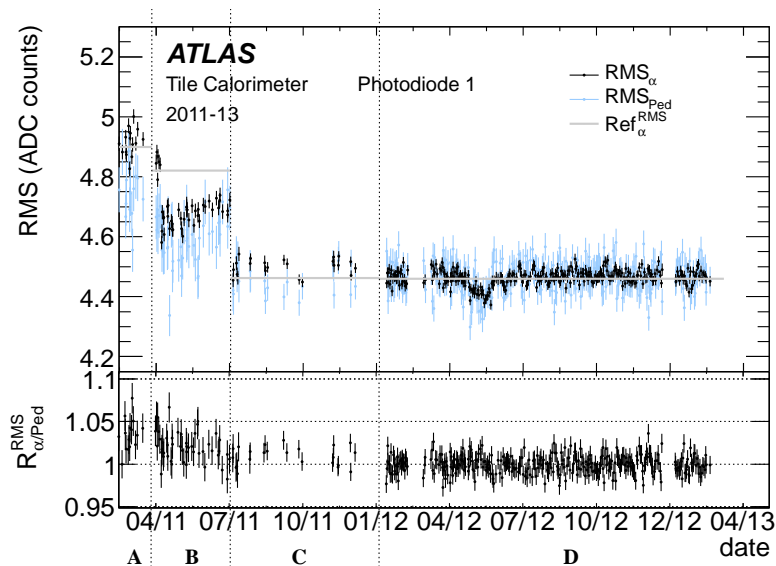
Figure 13. Evolution of the noise value measured in the Pedestals runs and in the Alpha runs, and their ratio for the first photodiode from February 2011 to February 2013. The error bars represent the statistical uncertainties on the averages and the ratios.

In conclusion, the readout electronics is found to be stable since April 2011. Evolutions of the pedestal, probably due to environmental effects like temperature and humidity, is not a problem since the value measured regularly in the Pedestals runs can be used for the response renormalisation in the Alpha and Laser runs. Moreover the electronic noise is perfectly stable and similar in different types of runs.
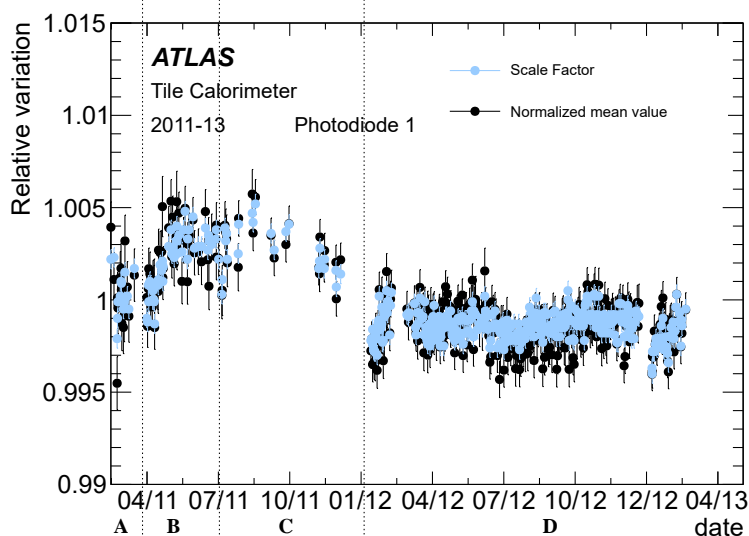
Figure 14. Evolution of the scale factor and the normalised mean value of the α spectra from February 2011 to February 2013. The error bars represent the statistical uncertainties.

For the rest of this article, the response of the photodiodes will always be the value after pedestal subtraction.

3.2 Calibration of the photodiodes

In the Laser calibration of the TileCal, the photodiodes are necessary to measure the intensity of each Laser pulse sent to the calorimeter PMTs, thus requiring that the response of the photodiodes to a given energy does not vary with time. The monitoring of this potential evolution is performed by depositing a known amount of energy periodically in the photodiodes, i.e. α particles of 5.6 MeV, using the Alpha runs.

Two methods have been used to study the evolution of the response of the photodiodes to α particles. In both methods, a high statistics Alpha run is used as a reference and each Alpha run is compared to this reference. Four reference runs have been defined, each one at the beginning of a period as defined in the previous section. The reference run for period C contains 3.8×10^5 α events and the reference run for period D 1.1×10^6 events.

The first method is using the *normalised mean value* that consists in computing the ratio between the mean value of the α spectrum in the Alpha run under study with the mean value of the α spectrum in the reference run.

The second method has been developed specifically for this study. It is called the *scale factor* and it is based on the assumption that the variation in the measured α spectra is due to a variation of the gain of the photodiodes and/or their readout electronics, thus only implying a rescaling of the spectra and not a distortion. Therefore, in this method, the spectrum under study is compared to the reference spectrum. A test spectrum is first built by rescaling the reference one, i.e. by multiplying the photodiode response for each recorded event by a constant number, called the scale factor. Then, this test scale factor is varied until the resulting distribution fits as well as possible the α spectrum under study, using the Kolmogorov-Smirnov test [19, 20]. The resulting scale factor

is then a measurement of the gain variation, being equal to one if no rescaling is needed to fit the reference distribution to the studied one.

To compare the two methods and their sensitivity to pedestal and noise variations, studies with simulated α spectra were performed. These simulated α spectra were generated by randomly drawing photodiode responses, according to a measured high statistics α distribution. Then, these simulated α spectra were shifted (to simulate a pedestal variation), rescaled (to simulate a gain variation) or smeared (to simulate an increase of the noise), before being used as input to the photodiode calibration procedure. These studies have shown that the scale factor method has a smaller uncertainty (0.05 %) than the normalised mean value (0.1 %). Moreover, they have also shown that the bias introduced by a wrong measurement of the pedestal is the same for the two methods: if the true pedestal differs from the subtracted one by x %, the bias is $0.2 \times x$ %. Finally, as has been shown in the previous section, the noise in the Alpha runs may be up to 5 % larger or smaller than in the Pedestals runs. The simulation showed that an error of 5 % on the noise would bias the scale factor by a negligible amount (0.0003 %) and would have no measurable effect on the normalised mean value. The noise measured in the reference runs ($\text{Ref}_\alpha^{\text{RMS}}$) can be seen on figure 13 as the horizontal lines and shows a good agreement with the noise measured in the studied Alpha runs. Therefore, the scale factor is chosen as the main method to study the evolution of the response of the photodiodes, with the normalised mean value as a cross-check.

Figure 14 shows the evolution of the normalised mean value and the scale factor measured in the Alpha runs. It appears that the period D was more stable than the previous ones. Concentrating on the scale factor, the largest variation is 0.6 % in the periods C and D and usually even less, which is small enough to safely use the response of the photodiodes to Laser pulses as a reference.

4   Calibration of the calorimeter

As has been seen in equation (1.1), the reconstruction of the energy in TileCal depends on several constants, some of them being updated regularly. The main calibration of the TileCal energy scale is obtained using the Cesium system [2]. However, since a Cesium scan needs a pause in the proton-proton collisions of at least six hours, this calibration cannot be performed very often. Therefore, regular relative calibrations are accomplished between two Cesium scans using the Laser system. The method to compute the Laser constant f_{Las} introduced in equation (1.1) is based on the analysis of specific Laser calibration runs, taken about twice a week, for which both the Laser system photodiodes and the TileCal PMTs are readout. By definition, if the response of a channel to a given Laser intensity is stable (the gains of the PMT and of the associated readout electronics are stable), the Laser constant f_{Las} is 1.

In the next sections, the general method to determine these Laser calibration constants f_{Las} is first described, the uncertainty on these constants is then estimated, followed by the description of the actual procedure to produce them.

4.1   Description of the method

A Laser calibration consists in two successive runs:

- a Low Gain run (labelled LG) with 10^4 pulses using the filter with an attenuation factor of 3,

- a High Gain run (labelled HG) with 10^5 pulses using the filter with an attenuation factor of 330.

For each type of run, $R_{i,p}$ is defined as the normalised response of channel i:

$$R_{i,p} = \frac{E_{i,p}^{\text{pmt}}}{D1_p} \tag{4.1}$$

where, for the pulse p, $D1_p$ is the signal measured in the photodiode 1[8] in the Laser box and $E_{i,p}^{\text{pmt}}$ is the signal measured by the TileCal photomultiplier connected to the channel i. The analysis is performed with the mean value of this ratio over all pulses for each channel, denoted $R_i = < R_{i,p} >$.

The Laser calibration is a relative calibration with respect to a Laser reference run taken right after each Cesium scan. The raw relative gain variation of a channel i is defined as follows:

$$\Delta_i = \frac{R_i - R_i^{\text{ref}}}{R_i^{\text{ref}}} \tag{4.2}$$

where R_i^{ref} is the normalised response of the TileCal channel i during the reference Laser run.

However, due to inhomogeneities in the light mixing of the light splitter or radiation damage to the long clear optical fibres, the light intensity may vary with time and from fibre to fibre (one fibre being linked to half of the PMTs of the same TileCal module). Therefore, Δ_i is corrected by the term $\Delta_{f(i)}^{\text{fibre}}$ ($f(i)$ is the number of the fibre coming from the Laser and connected to the given channel i) taking into account the gain variation due to a light variation of this specific fibre, as explained in the next paragraph.

To compute $\Delta_{f(i)}^{\text{fibre}}$, an iterative method is used. First, the distribution of Δ_i of channels fed by the same fibre is considered (see figure 15). In this distribution, only PMTs connected to the D cells for the long barrel modules and the B13, B14, B15, D5 and D6 cells for the extended barrel modules are used, assuming that these selected channels are stable between two Cesium scans.[9] The mean and the RMS of the Δ_i distribution are then calculated from these selected channels. To deal with single drifting channels that would bias the measurement of the shift due to the fibre itself, an iterative procedure is applied: all the channels that have a gain variation larger than twice the RMS are excluded from the distribution for the next iteration. The mean gain variation after five such iterations is the correction $\Delta_{f(i)}^{\text{fibre}}$.

The aim of this method is to correct the drifting channels of TileCal, not the variations of the fibres or any global variation. Therefore, the correction factor, f_{Las}^i for channel i, is defined as:

$$f_{\text{Las}}^i = \frac{1}{1 + \Delta_i - \Delta_{f(i)}^{\text{fibre}}} \tag{4.3}$$

and is the Laser calibration constant that enters in equation (1.1).

---

[8]The photodiode 1 is the one that measures the light right after the semi-reflecting mirror. The three other photodiodes have not been used in this method because several hardware interventions occured during the two years, affecting the optical fibres connected to these diodes.

[9]Since the D cells are the most distant cells from the interaction point, they are less affected by the radiations from the proton-proton collisions, unlike A cells that are more sensitive to the high light dose. The level of radiations has been validated using the minimum bias current measurements. The evolution of these cells between two Cesium scans has been checked from the evolution of the Cesium calibration constants and this evolution is well below 1%.
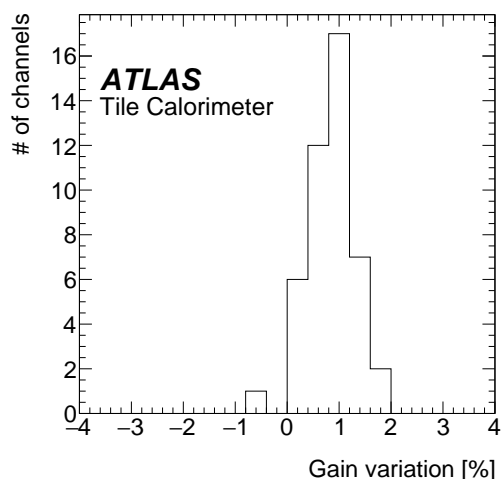
Figure 15. Example of distribution of Δ_i for all channels connected to one fibre. The average of this distribution is $\Delta_{f(i)}^{\text{fibre}}$ (see text).
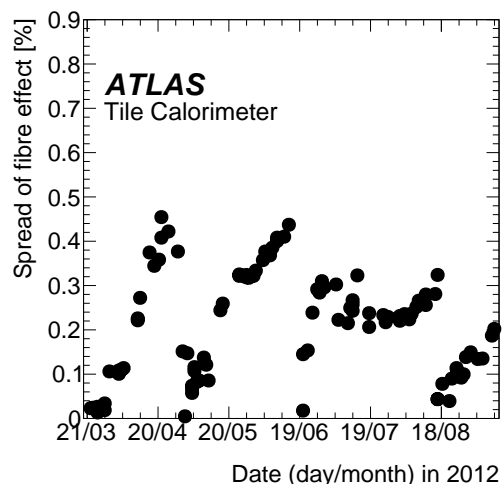
Figure 16. Inhomogeneity due to light distribution instabilities as a function of time.

4.2 Evolution of the fibre correction

Figure 16 gives a hint of the inhomogeneity of the light distribution during year 2012, estimated as the RMS of the distribution of all the $\Delta_{f(i)}^{\text{fibre}}$ with respect to the latest Laser reference run. At the beginning of each period, i.e. after each Cesium scan, the spread of the fibre correction factor determination is 0 by definition and it increases up to 0.4 % in a one month period.

4.3 Uncertainty on the correction factor

The method assumes that the reference D and B cells are stable. Systematic effects on the correction factor may arise, in particular from global variations of the PMT gains of these cells, due to two effects. The first effect, independent of the presence or absence of collisions, is a constant increase of the gains, but it is negligible over a period of one month (less than 0.1 %) and has been first observed in 2009 by the Cesium system, prior to collisions. The second effect, observed during collisions, is a decrease of the gains. Its origin is not completely understood but the effect is less than 0.5 % between two Cesium scans.

Assuming that the scintillators ageing is negligible between two Cesium scans (typically one month) and taking into account the fact that the precision of Cesium calibration constants is at the per-mil-level, the Cesium system is a good tool to determine the precision and the systematic uncertainty connected with the Laser calibration constants. The two systems are expected to provide compatible measurements. To compare the Laser and the Cesium calibration constants, pairs of the closest Laser run/Cesium scan are selected.

For each pair of Laser run/Cesium scan, the ratio of Laser calibration constants f_{Las} and Cesium calibration constants f_{Cs} is considered. In this comparison, are considered only the channels for which the quality of the two calibration constants is good. The distribution is fitted to a Gaussian function. The mean obtained by the fit quantifies the compatibility of the two calibration systems and its difference to one (called δ) is interpreted as the systematic uncertainty on the Laser calibration
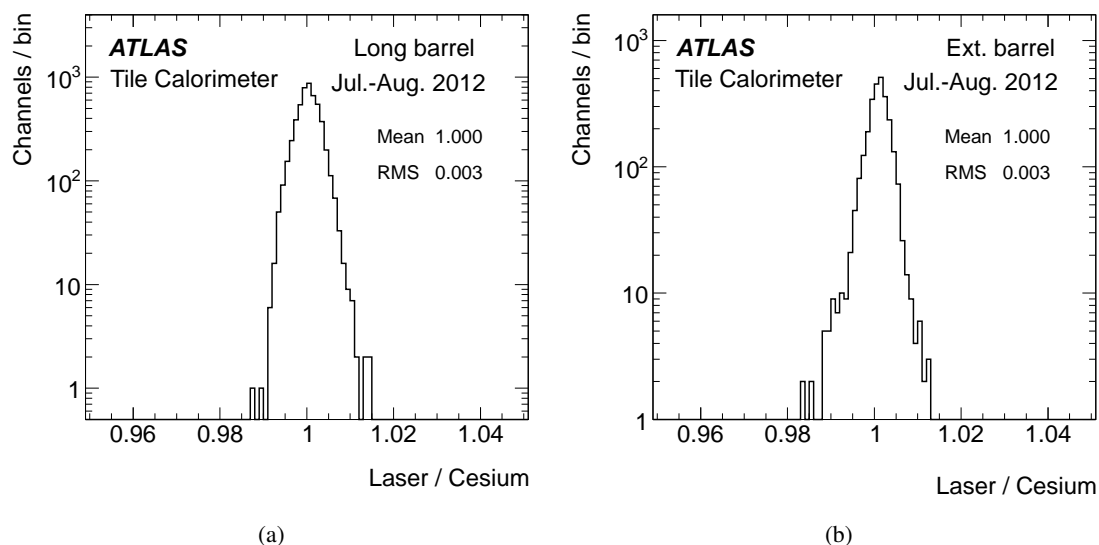
Figure 17. Example of distribution of the ratio $f_{\text{Las}}/f_{\text{Cs}}$ during one month for the long barrel (a) and the extended barrels (b). The runs were taken in July 9th and August 5th, 2012.

Table 1. Difference between the mean and unity (δ) and spread (σ) of a Gaussian fit to the distribution of the ratio $f_{\text{Las}}/f_{\text{Cs}}$ during 2012. The value of δ is always positive, due to the fact that the reference cells, that are assumed to be stable, have nonetheless a small decrease of the gain, yielding a systematic effect.

Period	Long barrel		Extended barrel	
	δ in %	σ in %	δ in %	σ in %
Mar 18-Apr 27	0.20 ± 0.01	0.29	0.29 ± 0.01	0.29
Apr 28-Jun 18	0.21 ± 0.01	0.30	0.56 ± 0.01	0.36
Jun 18-Jul 9	0.20 ± 0.01	0.27	0.40 ± 0.01	0.27
Jul 10-Aug 4	0.10 ± 0.01	0.26	0.10 ± 0.01	0.24
Aug 5-Aug 16	0.10 ± 0.01	0.27	0.10 ± 0.01	0.25
Aug 17-Sep 11	0.0 ± 0.01	0.27	0.10 ± 0.01	0.25
Sep 11-Sep 20	0.10 ± 0.01	0.26	0.30 ± 0.01	0.22
Sep 22-Oct 9	0.02 ± 0.01	0.26	0.05 ± 0.01	0.24
Oct 10-Nov 3	0.03 ± 0.01	0.28	0.13 ± 0.01	0.29
Nov 6-Dec 4	0.20 ± 0.01	0.24	0.30 ± 0.01	0.25
Dec 7-Dec 10	0.0 ± 0.01	0.36	0.40 ± 0.01	0.46

constants. The σ obtained by the fit can be interpreted as the statistical precision of the Laser system assuming that the uncertainty on the Cesium calibration constants is negligible with respect to the Laser one (it is therefore a conservative estimate of the Laser system precision).

Figure 17 shows a comparison between Laser and Cesium calibration constants, the ratio $f_{\text{Las}}/f_{\text{Cs}}$, for long and extended barrels, for a one month period in 2012. Fitting the same distributions for 11 periods in 2012 (see results in table 1), the systematic uncertainty on f_{las} is evaluated to be at most 0.21 % for the long barrel and 0.56 % for the extended barrels, and the statistical uncertainty

of the Laser system varies between 0.22 % and 0.46 %. The second period corresponds to a period of high LHC luminosity. As anticipated, this high luminosity has a more significative effect on the PMTs of the extended barrels than on the ones of the long barrel, as can be seen from table 1. The statistical and systematic uncertainties of the correction factors obtained using the Laser system are then estimated:

- statistical uncertainty: 0.3 %

- systematic uncertainty for long barrel: about 0.2 %

- systematic uncertainty for extended barrels: about 0.5 %

Combining together these results, the overall precision is estimated to be 0.4 % and 0.6 % for the long and the extended barrels respectively. However, the precision on the Cesium calibration constants (of the order of 0.2 %) is not completely negligible with respect to the Laser ones, thus the above values must be considered as upper limits rather than exact values.

4.4   Determination of the calibration constants

In equation (1.1), f_{Las} represents the correction of the PMT gain variation computed with the Laser system. However, only channels that have undergone a significant deviation are corrected, i.e. the value of f_{Las} is set to 1 if it is smaller than a predetermined threshold of about three times the overall precision of the Laser system, thus a threshold of 1.5 % for the long barrel and 2 % for the extended barrels. The low gain (LG) and the high gain (HG) Laser runs are used to determine the Laser calibration constants. However, the LG data are more precise than the HG data because the HG signal amplitude is much smaller than the LG one (a factor 100 between them for the same channel). Therefore, the LG Laser calibration constants are used for both gains, while the HG Laser calibration constants are used for cross-checks. A readout electronics issue can be revealed by an incompatibility between the LG and the HG Laser calibration constants.

Therefore, the production of the Laser calibration constants f_{Las} follows this procedure:

- for each pair of the LG and the HG runs, a Laser calibration constant is computed,

- a channel is corrected if its LG gain variation is larger than 1.5 % (2 %) in the LB (EB),

- the compatibility of the Laser calibration constants for the LG and the HG is required (both constants with same sign and above the thresholds), otherwise the Laser calibration constants are set to 1 — this is to ensure the calibration constant corrects only drifts due to the PMTs and not problems in the readout electronics itself that are covered by the CIS,

- a limit is applied to the constants values corresponding to a deviation between -60 % and +60 %. A healthy channel is not supposed to drift up to these values. However, a variation of up to -90 % is allowed for channels in a module in reduced-HV mode,[10]

---

[10]During the so-called reduced-HV mode of a module, the High Voltages (HV) regulation loop is turned off and then the HV applied to each PMT is lower, preventing high trip rate. The PMT gain is sensitive to variations of HV, so if the HV of the PMT decreases, the PMT gain will also decrease and will be very low (~-60 %) with respect to PMTs supplied with nominal HV.

- if a channel is known as bad, its Laser calibration constant is set to 1, whatever is the nature of the problem. Indeed, this flag is very often due to readout electronics, a gain variation or drift faster than Laser run frequency, or corrupted data, and the Laser system is not presumed to correct these cases.

Based on these criteria, only 60 channels among $\sim 10^4$ could not be corrected by the Laser system during the LHC run 1.

A few additional conditions are needed for three different types of channels: the ones linked to the E3 and E4 cells, the channels in reduced-HV modules and some channels that have an erratic behaviour, likely due to readout electronics problems. These latter channels are not calibrated.

The channels linked to E3 and E4 cells are not calibrated by the Cesium system, while the Laser system monitors all the TileCal channels, including those connected to these special cells. The fact that there is no Cesium calibration implies that there are no references for these channels. The chosen solution is to monitor these channels and provide constants with respect to a reference date set to March 18th 2012 which is the date of the first Laser reference run in 2012. Even though the precision of the Laser system over a period of one year has been estimated to be less than 2 %, it is sufficient to calibrate these highly drifting cells.

Some reduced-HV modules can not be calibrated by the Cesium system. As for the E3 and E4 cells, these channels are monitored and Laser constants are computed starting from the Laser reference run taken just before the beginning of the reduced-HV mode period.

Finally, the channels linked to E1, E2 cells[11] and MBTS (see section 1.1) are not corrected by the Laser system.

Over the large number of runs recorded and analysed in 2012, only 32 pairs of Laser runs were needed to calibrate the data. Indeed, if several consecutive runs lead to compatible constants, only the constants from the first pair are implemented for the full period. The main periods during which a large number of channels had to be calibrated (at most 432 in the long barrel and 148 in the extended barrels) are at the end of April and the beginning of June 2012. Indeed, during these periods high luminosity was delivered by LHC, producing high current in the PMTs, thus modifying their gain. Other channels that needed calibration in 2012 were the 224 channels reading the E3 and E4 cells as well as the 167 channels of the reduced-HV mode modules.

4.5   Calibration with pulses during physics runs

Up to now, the Laser calibration constants have been computed using dedicated Laser calibration runs, recorded on a regular basis between collision runs. But, as explained in section 2.6, the Laser pulses are also emitted during collision runs, and are used only so far to monitor the calorimeter timing (see section 5). However, with the increase in instantaneous luminosity expected from the LHC, resulting in possible fast variations of the gains of the TileCal PMTs during collisions, being able to monitor these gains during the physics runs will become important. Technically, the main difference with standard Laser runs is that the number of Laser events is not fixed, since it depends on the length of the physics run and therefore on the beam conditions. An additional study

---

[11]The E1 and E2 cells are not calibrated by the Laser because their measured variation, smaller than for the E3 and E4 cells, is of the same order of magnitude as the Laser precision, due to a lower precision non-standard Cesium calibration (the Cs source cannot pass through these cells).

was performed and showed that, applying the method described in the previous paragraphs, Laser calibration constants can be derived with a good precision using these runs: the statistical precision with 5000 pulses, corresponding to a rather short physics run (85 minutes), is similar to a standard calibration run (0.3 %). Therefore, the physics runs will probably be used in the future to derive Laser calibration constants.

5 Timing monitoring and correction

The TileCal does not only provide a measurement of the energy that is deposited in the calorimeter, but also the time when this energy was deposited. This information is in particular exploited in the removal of signals that do not originate from proton-proton collisions as well as for time-of-flight measurements of hypothetical heavy slow particles that would enter in the calorimeter. Therefore, the time synchronisation of all calorimeter channels represents one of the important issues in the calibration chain.

5.1 Time reconstruction

As described in section 1.2, the signal coming from the PMTs is digitised every 25 ns and seven samples are readout after a positive level-1 trigger decision. The optimal filtering (OF) method that is applied on these samples is able to determine the total amplitude of the signal but also the signal phase, defined as the phase of the analog signal peak with respect to the TTC clock signal corresponding to the fourth sample. The precision on this measurement is better than 1 ns [2, 10]. The optimal filtering method is applied online to all channels and later re-computed offline in channels that have sufficiently large signals.

However, the parameters of the OF method depend on this signal phase, thus a bad setting of the timing of a channel will produce a wrong measurement of the signal amplitude. Studies have shown that a difference of 25 ns between the actual and supposed phases degrades the reconstructed energy by 35 %. For timing differences of a few nano-seconds, the effect on the measured energy is small but the corresponding cells could be excluded from the reconstruction, being falsely tagged as not coming from proton-proton collisions.

The PMT signal digitisation is performed by an electronic board called the digitiser that is able to process the signal from six PMTs. Only the timing of each digitiser can be adjusted independently of each other. Inside the digitiser the six channels have the same relative timing.

The meaurement of the pulse timing is made in two steps. First, the phases of the digitisers are set so that the physics signals from particles originated in the interaction point and travelling with the speed of light peak close to the fourth sample. Second, the residual offsets t_{phase} are measured, using dedicated runs, as the average of the reconstructed OF time t_{OF}. The channel time is then defined as $t_{channel}^{phys} = t_{OF} - t_{phase}$. This value should of course be close to zero for standard particles coming from the interaction point at nearly the speed of light.

5.2 Timing jumps

During data taking, it was discovered that digitisers can suddenly change their timing settings due to a mis-configuration, either at the beginning of a run or after an automatic power cycling of the low voltage power supplies (LVPS) feeding the TileCal front-end electronics. This mis-configuration of
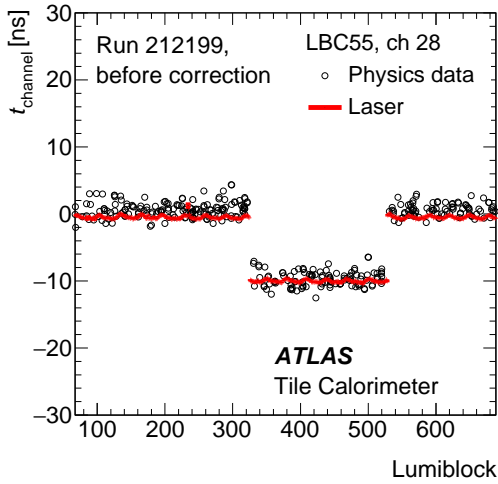
Figure 18. Example of measured channel time as a function of time during a single ATLAS run, comparing timing from physics events and from Laser calibration events, exhibiting a timing jump.
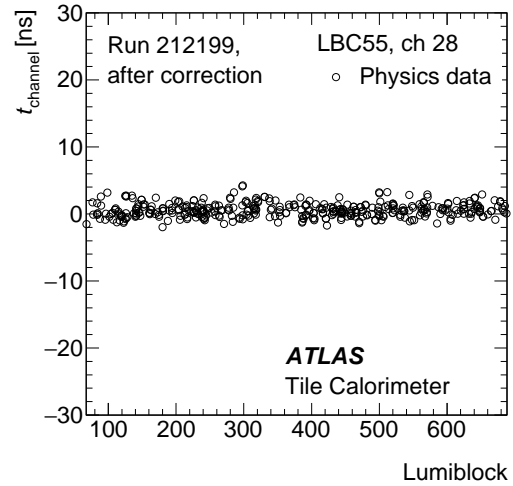
Figure 19. Example of reconstructed time from physics events after correcting for the timing jump.

the time settings is later referred to as timing jump. An example of such a behaviour can be seen in figure 18 where the reconstructed time for a channel is represented as a function of the luminosity block, that is the elementary unit of time in a run (one or two minutes depending on data taking periods) for which parameters like calibration constants can be modified if necessary. Of course, this kind of feature has a negative impact on the calorimeter performance since the reconstructed energy and time are mis-measured during the period affected by the timing jump.

As stated previously, the Laser system emits light pulses also during physics runs. Since all calorimeter channels are exposed to Laser light at the same time, the statistics is sufficient to determine the reconstructed time to a precision of about 1 ns. Because the Laser is not synchronised with the LHC clock, the reconstructed time in each channel must be corrected for the Laser phase using the Laser TDC information t_{TDC}. In addition, the time of arrival of the Laser pulses to the TileCal PMTs is different from the signal time for particles from collisions, due to the path followed by the Laser light. Therefore, in a channel perfectly timed-in for physics, the Laser pulse arrives at a different time[12] t_{ref}^{laser}. The channel time for Laser events is then defined as $t_{channel}^{laser} = t_{OF} - t_{TDC} - t_{ref}^{laser}$. If the time setting of the digitiser is correct, $t_{channel}^{laser}$ should be close to zero.

The Laser events are recorded in parallel to the physics data taking and this stream gets reconstructed immediately once the run finishes. The reconstructed Laser times $t_{channel}^{laser}$ are histogrammed for each channel as a function of the luminosity block. Since this time is supposed to be close to zero, the monitoring program searches for differences from this baseline. Identified cases — potential timing jumps — are automatically reported to the data quality team for manual inspection. If the timing jump is confirmed, the t_{phase} value of the corresponding channel is modified for the affected period, thus allowing to recover a correct reconstructed time, as demonstrated on figure 19. These Laser results are available still during the calibration loop and thus allow for time constants correction before the full data processing starts.

---

[12]The reference Laser time t_{ref}^{laser} represents the mean value of t_{OF} corrected for the Laser TDC on the per-event basis.
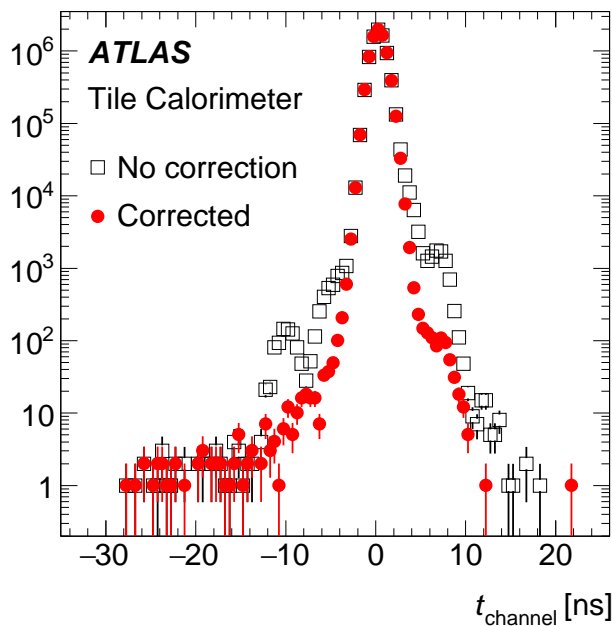
Figure 20. The impact of the timing jump corrections on the reconstructed channel time in jet collision data. Shown are all TileCal high gain channels with $E_{channel} > 4$ GeV, being a part of reconstructed jets. Data correspond to 1.3 fb^{-1} of collected physics data in 2012.

Almost all timing jumps detected with Laser events can be corrected during the subsequent data processing. However, few digitisers appeared to be very unstable, exhibiting very large number of timing jumps. Such channels are flagged as *bad timing*. This flag prevents the time from such channels to be used in the further physics object reconstruction.

5.3 Impact of the timing jumps on the calorimeter time performance

The overall impact of the timing jump corrections on the reconstructed time was studied with jet collision data using a sub-set of the 2012 data representing 1.3 fb^{-1} of collected physics data. To reduce the impact of the time dependence on the reconstructed energy, the channel energy was required $E_{channel} > 4$ GeV, but still read out with high gain.[13]

The results are displayed in figure 20, where the reconstructed time is shown for all calorimeter channels with and without the timing jump corrections. While the Gaussian core, corresponding to channels (and events) not affected by timing jumps, remains basically unchanged, the timing jump corrections significantly reduce the number of events in the tails. The overall RMS is improved by 9 % (from 0.90 ns to 0.82 ns after the corrections are applied).

6 Pathological channels monitoring

For a few channels, the monitoring shows that the PMT input high voltage is unstable. This instability may be due to a true unstable input voltage or a failure of the monitoring system. In order

---

[13]This is important since the high gain response is delayed with respect to that of low gain by about 2 ns. The high gain requirement imposes an effective upper limit of about $E_{channel} < 12$ GeV.
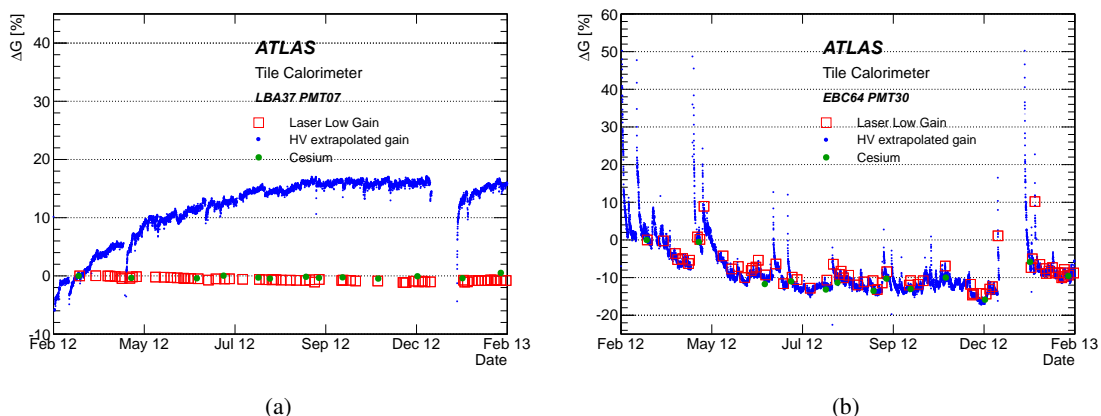
Figure 21. Example of pathological channels monitoring in 2012. These plots present the comparison between the gain variation expected from the high voltage monitoring (blue dots) and the one measured by the Laser (red squares) and the Cesium (green dots) systems. The vertical structures are due to ON/OFF switchings and are expected. However, between two switchings and for normal channels, the gain should be constant.

to disentangle the two possibilities, the Laser system can be used to measure the real gain variation (as described in the previous sections). Figure 21(a) presents an example of such pathological channel behaviour. In this case, the Laser system does not observe any variation of the PMT gain, meaning that the actual input high voltage must be stable and the drift observed in the monitoring is not real. In the case of figure 21(b), the Laser system confirms the instability of the high voltage distribution system, the very large gain variations measured by the Laser system being in agreement with the variations computed from the high voltage monitoring.

7 Conclusions

The Laser system is one of the three calibration systems of the ATLAS Tile Calorimeter. It is a key component for monitoring and calibrating the 9852 TileCal photomultipliers and their associated readout electronics. The Laser calibration constant f_{Las} applied on each channel has been regularly measured, with a statistical uncertainty at the level of 0.3 %, and is one ingredient in the TileCal cell energy reconstruction. Comparing these correction factors with the ones derived with the Cesium calibration system, a good compatibility between them was found and the systematic uncertainty on the Laser calibration constants is estimated to be 0.2 % for the long barrel modules and 0.5 % for the extended barrel modules. The Laser system has also been used to monitor the timing of the TileCal front-end electronics during physics runs, allowing to correct for timing jumps provoked by mis-configuration resulting from power supplies trips. It has also been used to monitor the behaviour of pathological calorimeter channels.

In order to improve the stability and the reliability of the system for the LHC run 2, a major upgrade was performed in October 2014, including a completely new electronics, ten photodiodes to measure the light at various stages in the Laser box, and a new light splitter.

References

[1] ATLAS collaboration, *The ATLAS Experiment at the CERN Large Hadron Collider*, 2008 *JINST* **3** S08003.

[2] ATLAS collaboration, *Readiness of the ATLAS Tile Calorimeter for LHC collisions*, *Eur. Phys. J.* **C 70** (2010) 1193 [arXiv:1007.5423].

[3] ATLAS collaboration, *ATLAS tile calorimeter: Technical Design Report*, CERN-LHCC-96-042 (1996).

[4] K. Anderson et al., *Design of the front-end analog electronics for the ATLAS tile calorimeter*, *Nucl. Instrum. Meth.* **A 551** (2005) 469.

[5] S. Berglund et al., *The ATLAS tile calorimeter digitizer*, 2008 *JINST* **3** P01004.

[6] J. Poveda et al., *ATLAS TileCal read-out driver system production and initial performance results*, *IEEE Trans. Nucl. Sci.* **54** (2007) 2629.

[7] W.E. Cleland and E.G. Stern, *Signal processing considerations for liquid ionization calorimeters in a high rate environment*, *Nucl. Instrum. Meth.* **A 338** (1994) 467.

[8] A. Valero on behalf of the ATLAS Tile Calorimeter system, *The ATLAS TileCal Read-Out Drivers Signal Reconstruction*, *IEEE Nucl. Sci. Symp. Conf. Rec. (NSS/MIC)* (2009) 593.

[9] E. Starchenko et al., *Cesium monitoring system for ATLAS Tile Hadron Calorimeter*, *Nucl. Instrum. Meth.* **A 494** (2002) 381.

[10] P. Adragna et al., *Testbeam studies of production modules of the ATLAS tile calorimeter*, *Nucl. Instrum. Meth.* **A 606** (2009) 362.

[11] Z.J. Ajaltouni et al., *The Tilecal laser monitoring*, Tech. Rept. ATL-TILECAL-94-039, ATL-L-PN-39 (1994).

[12] P. Grenier and L. Says, *Analysis of the 1997 test beam laser data of the Tilecal extended barrel module 0*, Tech. Rept. ATL-TILECAL-98-159 (1998).

[13] Photo-diode S3590-08 from Hamamatsu, https://www.hamamatsu.com/resources/pdf/ssd/s3590-08_etc_kpin1052e.pdf.

[14] R. Alves, J. Carvalho, Y. Ivaniouchenkov, J. Mateu, F. Moita and J. Pinhão, *The distribution of laser light for the calibration and monitoring system of the ATLAS hadronic calorimeter*, *IEEE Nucl. Sci. Symp. Conf. Rec.* (1999).

[15] K. Aitamar et al., *Optical fibre connectors for the laser calibration system*, Tech. Rept., ATL-TILECAL-96-093 ATL-L-PN-93 (1996).

[16] TTCrq web site, http://proj-qpll.web.cern.ch/proj-qpll/ttcrq.htm.

[17] High-speed Optical Link for Atlas web site http://hsi.web.cern.ch/HSI/s-link/devices/hola/.

[18] L. Evans and P. Bryant, *LHC Machine*, 2008 *JINST* **3** S08001.

[19] A. Kolmogorov, *Sulla determinazione empirica di una legge di distribuzione*, *G. Ist. Ital. Attuari* **4** (1933) 83.

[20] N. Smirnov, *table for estimating the goodness of fit of empirical distributions*, *Ann. Math. Statist.* **19** (1948) 279.